Journal of Materials Chemistry C

ROYAL SOCIETY OF CHEMISTRY

PAPER

Published on 17 August 2026

Cite this: DOI: 10.1039/d6tc01477a

Synthesis-directed morphological control of NiO_x nanomaterials: the role of base, precursor, and calcination temperature

Weitao Qian, [a] Zhaoyi Du,[a] Longren Li, [b] Gwilherm Kerherve, [c] Yanhao Sun,[c] Milo S. P. Shaffer [bc] and Martyn A. McLachlan *[a]

Nickel oxide (NiO_x) nanoparticles are widely studied as earth-abundant p-type metal oxide semiconductors, and numerous applications spanning emerging electronic, optoelectronic and energy-related devices have been proposed. In this work, we systematically investigate the impact of modifying the nickel precursor, precipitating base and calcination temperature on the formation of NiO_x *via* a chemical precipitation synthesis, identifying the critical role of intermediate phases in controlling final product morphology. We investigate the products prepared by precipitating nickel acetate/nitrate with sodium hydroxide/bicarbonate and show that the intermediates formed, crystalline nickel hydroxide ($Ni(OH)_2$) or amorphous basic nickel carbonate ($Ni_m(OH)_n(CO_3)_p$), are directly governed by the choice of base. The morphology of the intermediates is further dependent on the nickel precursor; the crystalline $Ni(OH)_2$ prepared from $Ni(NO_3)_2$ yields flake-like structures, whilst $Ni(OAc)_2$ results in spherical particles and those precipitated using $NaHCO_3$ result in spherical particles. Thermal analysis of the intermediates reveals the temperature range of their degradation and subsequent NiO_x formation, with calcination carried out at 270, 450 and 650 °C. The spherical intermediates retain this morphology; however, they progressively coarsen with increasing temperature, whilst the flake-like structures evolve into ring-like features at 450 °C that then fragment at 650 °C. Overall, our results establish clear links between the precursor chemistry, intermediate-phase formation, and decomposition pathway during calcination, demonstrating how these stages collectively govern the structure, surface structure chemistry and morphology of the resulting NiO_x. These findings provide a practical framework for rationally tuning NiO_x powders through low-complexity, wet-chemical processing, and are also relevant to the broader preparation of metal oxide nanomaterials.

Received 8th May 2026,
Accepted 9th August 2026

DOI: 10.1039/d6tc01477a

rsc.li/materials-c

Introduction

Nanoscale nickel oxide (NiO) structures, *e.g.* particles, sheets, spheres and flakes, have been widely explored for applications spanning energy conversion and storage, catalysis, sensing and more recently in biomedical and healthcare spaces.[1–5] Implementation across such a diverse spectrum of applications is possible owing to the unique combination of optoelectronic properties—governed by facile defect and stoichiometry tunability, excellent chemical stability, low toxicity and earth abundance—affording readily synthesised materials that can be prepared at low-cost and at scale.[6–8] NiO adopts a rock-salt structure, consisting of two interpenetrating face-centred cubic (fcc) sublattices of Ni^{2+} and O^{2-} ions. At room temperature NiO is an insulator, with a bandgap of 3.6–4 eV[9,10] and a low intrinsic carrier concentration; however, NiO commonly exhibits p-type semiconducting behaviour arising from its non-stoichiometry (thus NiO_x, where $x > 1$).[11,12] The origin of this behaviour is attributed to the formation of nickel vacancies ($V^{\bullet\bullet}_{Ni}$) that are compensated for by the oxidation of neighbouring Ni atoms ($Ni^{2+} \rightarrow Ni^{3+}$). The valence band (VB) comprises mostly of O 2p states hybridised with Ni 3d states, the conduction band (CB) being primarily Ni 3d like in character, thus the magnitude of the O 2p to Ni 3d transition governs the magnitude of the bandgap.[13,14] The formation of $V^{\bullet\bullet}_{Ni}$ occurs, and the resulting Ni^{3+} states lie near the top of the VB, enabling hole transport *i.e.* p-type semiconducting behaviour. Whilst there may be some oxygen vacancies ($V^{\bullet\bullet}_{O}$) present, they do not make an effective contribution to the conductivity, tending rather to localise on Ni

[a] *Department of Materials, Molecular Sciences Research Hub, Imperial College London, London, W12 0BZ, UK. E-mail: martyn.mclachlan@imperial.ac.uk*
[b] *Department of Chemistry, Molecular Sciences Research Hub, Imperial College London, London, W12 0BZ, UK*
[c] *Department of Materials, Royal School of Mines, Imperial College London, London, SW7 2AZ, UK*

sites, reducing the metal, rather than contributing to the CB. The incorporation of extrinsic dopants, *e.g.* Cu and Li, has been explored to increase the hole concentration, thus enhancing the p-type characteristics.[15,16] The case of Li is more straightforward, with Li^+ substituting Ni^{2+}, requiring charge compensation through oxidation to Ni^{3+} and increasing hole concentration. With Cu, the situation is more complex owing to the accessibility of both Cu^+ and Cu^{2+} oxidation states. Cu^+, induces charge compensation, analogous to LI^+ however isovalent doping with Cu^{2+} has little direct effect on the carrier concentration but can alter morphology. Careful control of processing conditions is therefore required to stabilise the desired oxidation state and optimise the effects of doping.[17–19]

With growing research activity focusing on tailoring the properties of thin-film and bulk NiO_x, there has been parallel interest in NiO_x nanomaterials, affording improvements in dispersibility in solution, creating pathways to large area deposition, as well as processing on flexible substrates.[9] Furthermore, the markedly increased surface-area-to-volume ratio achievable, reduced ion-diffusion lengths and enhanced specific capacitance combined with tuneable optical and magnetic behaviour make the pursuit of the controlled synthesis of NiO_x extremely desirable.[10,20–22] Indeed, controlling nanoscale morphology is crucial to continue making advances in sensing (surface area, porosity, facet exposure), energy storage (ion transport and structural stability) and charge transport (film continuity, microstructure, roughness). Consequently, a variety of strategies have been developed to prepare nanoscale NiO_x, which can be broadly divided into physical, biological, and chemical methods.[10,23] Pulsed laser ablation (PLA) and mechanical milling are among the physical methods, both regarded as top-down techniques *i.e.* reducing bulk materials to the nanoscale.[10] PLA generates ligand-free nanomaterials with clean surfaces that require no purification,[24] whereas mechanical milling is favoured for its simple operation and ease of scale-up.[25] Despite these merits, physical routes in general suffer from high energy consumption and expensive instrumentation requirements.[10,26] Biological and chemical routes instead follow bottom-up assembly, during which atoms or molecules assemble into nanoscale structures.[10] The biogenic synthesis is known for its sustainability, as plant extracts (*e.g.*, leaves, roots, fruits, flowers) or microbial extracts (*e.g.*, bacteria, algae, fungi) act as natural reducing, stabilizing, and capping agents.[10,23,27] Yet this green method is limited by the batch-to-batch variability of biological extracts, leading to poor reproducibility.[23] Within this context, chemical synthesis has emerged as a popular route for producing NiO_x nanomaterials, owing to its high yield, cost-effectiveness, scalability, and reproducibility. Notable examples include sol–gel, hydrothermal, thermal decomposition, microwave-assisted, and precipitation approaches.[9,10,12,23,26] Among these, hydrothermal synthesis is particularly effective for obtaining highly crystalline products with well-controlled size and morphology. Numerous morphologies have been reported in a diverse range of applications, for example nanoworms, nanorods, and nanoparticles being explored for photocatalytic applications,[28] flower-like architectures for enhanced gas-sensing,[29] and hexagonal flake-like structures for antibacterial studies.[30] Despite the versatility, such routes are energy and time intensive, requiring extended reaction times and the use of elevated temperature and pressure. In contrast, chemical precipitation offers process simplicity, scalability and—in principle—the ability to readily tune particle size and morphology.[26] However, the resulting NiO_x is commonly reported as irregular or particle-like, underscoring the limitation of this method in terms of morphological diversity.[31,32] Thus, morphological control of NiO_x relying on chemical precipitation remains challenging and the fundamental relationships between reaction conditions and final product morphologies remain largely unexplored.

Here, we systematically investigate the influence of the key parameters in the chemical precipitation synthesis of NiO_x, elucidating the role of the base, nickel precursor and calcination temperature in determining the structure, surface chemistry and morphology of a range of NiO_x nanomaterials. We find that the intermediates prepared have a composition that is directly controlled by the choice of base, with sodium hydroxide (NaOH) yielding crystalline nickel hydroxide ($Ni(OH)_2$) and sodium bicarbonate ($NaHCO_3$) producing amorphous basic nickel carbonate ($Ni_m(OH)_n(CO_3)_p$). The intermediates and calcined NiO_x all adopt a spherical morphology, except the product of $Ni(NO_3)_2$ precipitated with NaOH, which has a flake-like intermediate that is retained after low-temperature calcination, then evolves into a ring-like morphology and subsequently fragments at elevated temperature. By correlating reaction conditions with characteristics of both intermediate species and the oxide products, we develop a better understanding of the formation of NiO_x nanoparticles throughout the precipitation–calcination process.

Results and discussion

We employed a chemical precipitation route to prepare NiO_x nanomaterials, with the reaction pathway illustrated in Fig. 1, and the experimental parameters are summarised in Table S1. In this approach, a base is introduced into an aqueous nickel salt solution to generate an insoluble Ni-intermediate (eqn (1)), which *via* calcination is converted into NiO_x (eqn (2)). Understanding both processes is therefore essential for interpreting the properties of the final products.

$$\text{Nickel salt} + \text{Base} \rightarrow \text{Nickel intermediate} \quad (1)$$

$$\text{Nickel intermediate} \rightarrow NiO_x + \text{Volatile species} \quad (2)$$

Intermediate formation

We utilised two aqueous nickel solutions, obtained from nickel nitrate ($Ni(NO_3)_2$) and nickel acetate ($Ni(OAc)_2$), that were each precipitated using two bases, sodium hydroxide (NaOH) and sodium bicarbonate ($NaHCO_3$), creating four intermediate species. Both nickel precursors are soluble in water; however, for each, different anions will be formed during dissolution, namely NO_3^- and OAc^-. The bases differ considerably in base-strength, for NaOH $pK_b = 0.2$ and $NaHCO_3$ $pk_{b1} = 7.65$ ($HCO_3^- + H_2O \rightleftharpoons H_2CO_3 + OH^-$) and $pk_{b2} = 3.67$ ($CO_3^{2-} + H_2O \rightleftharpoons HCO_3^- + OH^-$).[33] The precipitated intermediates were washed with deionised water

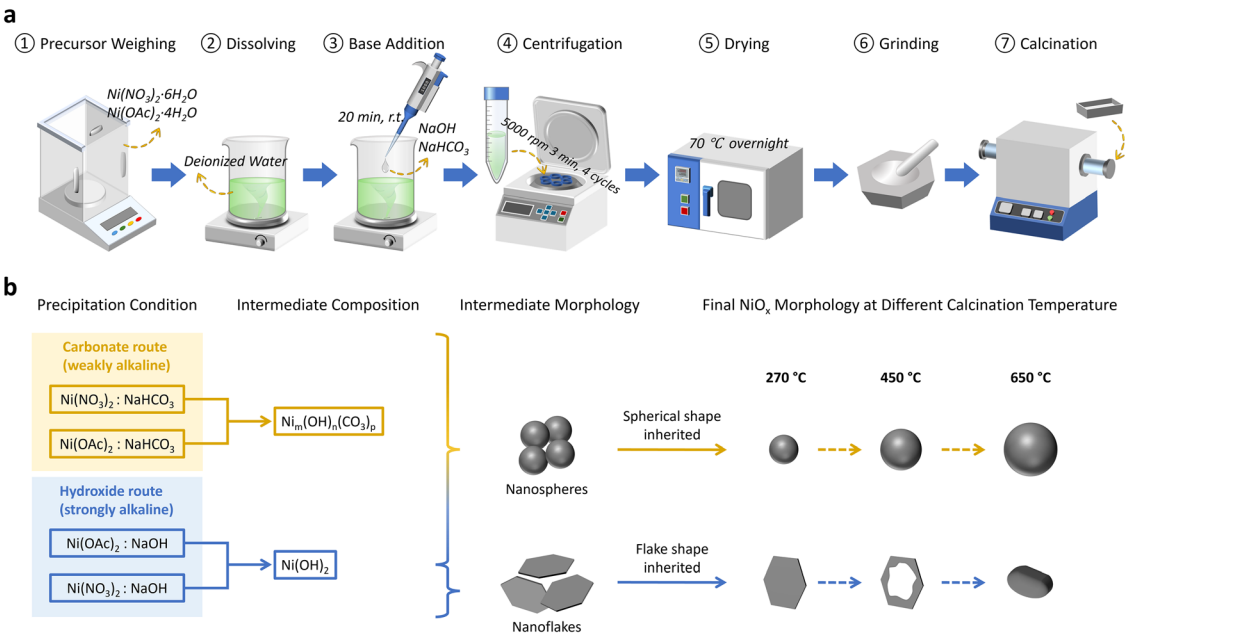

Fig. 1 (a) Schematic illustration of the chemical precipitation route used to synthesise NiO_x nanomaterials. The process begins with precursor solution preparation followed by base-induced precipitation, intermediate collection then washing, drying, grinding and final calcination to obtain NiO_x. (b) Proposed morphological inheritance mechanism for NiO_x formation, showing how the reaction conditions determine intermediate composition and morphology, which in turn dictate the morphology of the final product after calcination at different temperatures.

and oven-dried at 70 °C. The structure, surface chemistry and morphology of the intermediates prepared were comprehensively studied using a combination of scanning electron microscopy (SEM), Fourier transform infrared spectroscopy (FTIR), X-ray diffraction (XRD) and X-ray photoelectron spectroscopy (XPS).

Morphological comparison of the four intermediates was carried out using SEM, as shown in Fig. 2a, considering first the intermediates precipitated using NaOH. As a strong base, NaOH provides a high concentration of OH^- upon addition to the Ni^{2+} precursor solution, resulting in immediate supersaturation and precipitation, thereby generating many nuclei at the early stage of the reaction.[34,35] This rapidly lowers the concentrations of reactants, making further nucleation less favourable, with crystal growth becoming the dominant process.[36] With $Ni(NO_3)_2$ as the Ni source, flake-like structures (large lateral dimensions, low thickness) exhibiting an average in-plane size of 57.9 nm were observed. The corresponding XRD pattern, Fig. 2b, shows clearly defined, relatively sharp peaks that align with the reference pattern (ICDD: 00-059-0462), confirming the formation of a crystalline hydroxide phase with a layered structure. The relative increase in the intensity of the (101) diffraction peak relative to the (001) is consistent with the flake-like structure observed by SEM. In contrast, with $Ni(OAc)_2$ a spherical morphology is seen for the intermediate product, for which an average diameter of 25.8 nm was measured, and whilst the corresponding XRD data show overlap in peak position with the $Ni(NO_3)_2$: NaOH data the morphological differences mean that the influence of preferred orientation seen with $Ni(NO_3)_2$ are not seen here but there is obvious anisotropic broadening of the (001), (101), and (102) peaks.

The layered structure of $Ni(OH)_2$ results in strong in-plane bonding that maintains order; however, weaker interlayer interactions permit translations in the *a*- and *b*-planes and rotations along the *c*-axis.[37,38] It is clear that the conditions of the $Ni(NO_3)_2$: NaOH precipitation facilitate formation of the anisotropic, flake-like structures, consistent with the formation of β-$Ni(OH)_2$.[39] For the spherical particles prepared from $Ni(OAc)_2$: NaOH, the peak broadening is attributed to stacking faults.[40] Such disorder can be explained by considering the different coordination behaviour of the precursor anions. Specifically, acetate anions exhibit higher Lewis basicity than nitrate anions,[33,41] and the two oxygen donor sites make bidentate or bridging coordination possible,[42] enhancing the interaction with Ni^{2+}, thereby influencing the nucleation and crystal growth environment, disrupting anisotropic layer development, resulting in an intermediate with a sphere-like morphology.

When $NaHCO_3$ is used as the precipitating base distinct differences from the NaOH derived samples are observed in the SEM images, Fig. 2a, where independent of the Ni precursor, sphere-like particles are always prepared, with average particle sizes of 19.3 nm and 20.4 nm determined for the $Ni(NO_3)_2$ and $Ni(OAc)_2$ system, respectively. XRD characterisation, Fig. 2b, also shows distinct differences compared with the NaOH derived precipitates, where broad scattering is seen in the intermediates prepared from both Ni precursors, indicative of limited long-range order. We consider that the weaker basicity of $NaHCO_3$ results in slower precipitation kinetics because OH^- is supplied gradually through bicarbonate equilibria ($HCO_3^- \rightleftharpoons CO_2 + OH^-$). In addition, dissolution of $NaHCO_3$ generates multiple reactive species, including HCO_3^-, CO_3^{2-}, and OH^-, creating a more complex precipitation environment in which a range of precipitation reactions can occur.[33] Similar observations have been previously reported,[43,44] with the products described as amorphous;

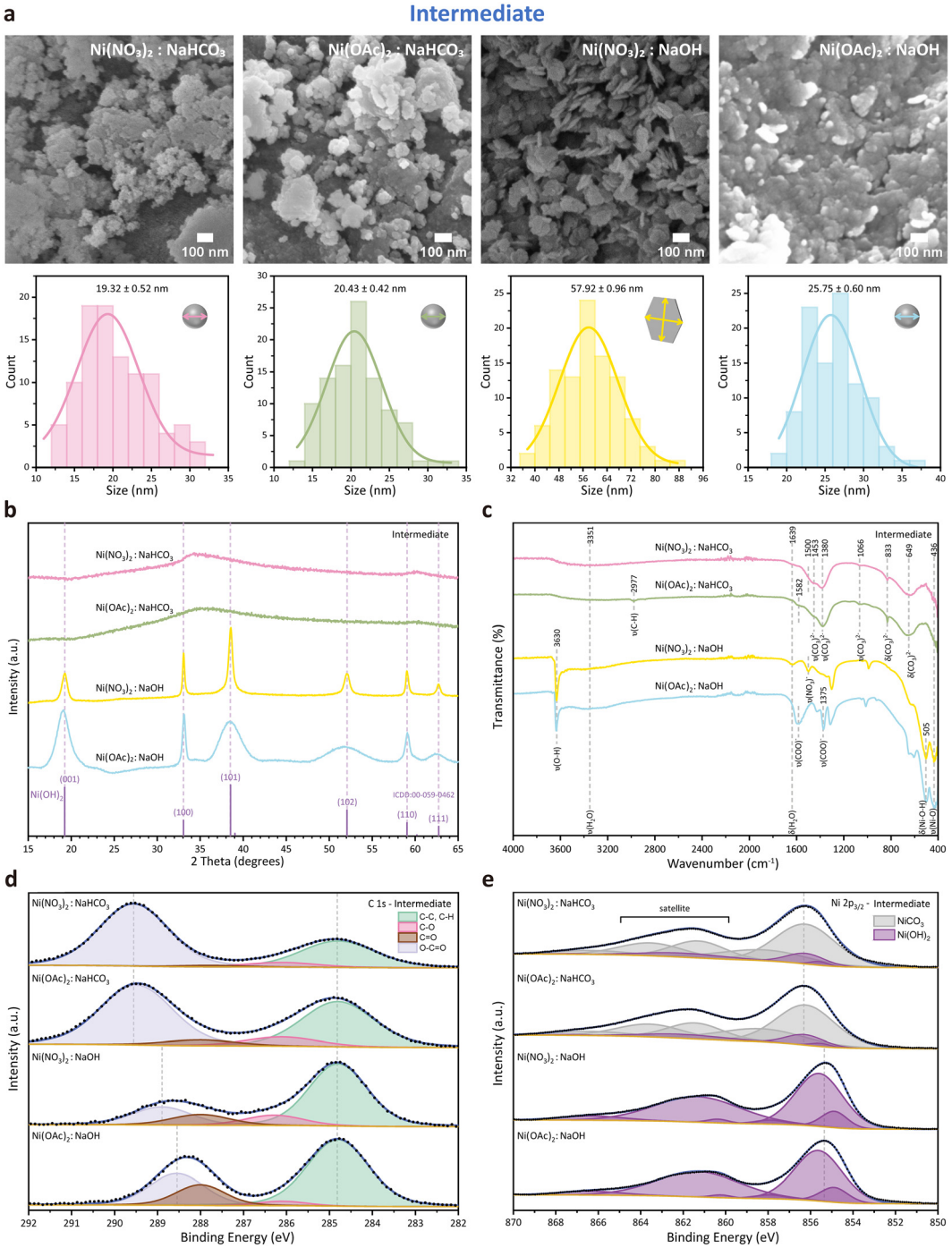

Fig. 2 Typical characterisation data obtained for the four intermediate species. (a) SEM images showing the range of morphologies formed, with the corresponding particle size distributions shown below. Particle sizes were measured according to the dimension indicated in the inset of each histogram. (b) XRD data for the intermediates; also shown is the matched $Ni(OH)_2$ pattern (ICDD: 00-059-0462). (c) FTIR spectra with the major vibrations labelled, and the fitted XPS data shown for (d) C 1s and (e) Ni $2p_{3/2}$ core level spectra. The fitting parameters are listed in Tables S2–S4.

however, their composition has not been determined; therefore, it is critical to determine the chemical composition of such intermediates, to better understand the precipitation processes and the resulting morphology, motivating further study.

Fourier transform infrared spectroscopy (FTIR) was used to identify the local bonding environment of the intermediates, as shown in Fig. 2c. All samples show bands centred around 3351 cm^{-1} and 1639 cm^{-1}, that can be assigned to the O–H stretching and bending modes of physiosorbed water respectively.[45–47] The bands at 436 cm^{-1} are assigned to Ni–O stretching, confirming the formation of nickel-oxygen bonds in all intermediates.[45,46] Despite such shared features there are distinct differences seen when the base is changed. When using NaOH the intermediates show a sharp band at 3630 cm^{-1}, characteristic of

lattice O–H stretching,[45–48] accompanied by a band near 505 cm^{-1} corresponding to Ni–O–H bending.[45–48] When combined, these absorptions reveal that using NaOH for precipitations leads to the formation of $Ni(OH)_2$, independent of the nickel precursor. In contrast, intermediates precipitated using $NaHCO_3$ show strong absorptions at 1453 and 1380 cm^{-1}, assigned to asymmetric C–O stretching with an accompanying band at 1066 cm^{-1} arising from the corresponding symmetric mode.[49–53] Additional bands located at 833 and 649 cm^{-1} originate from out-of- and in-plane O–C–O bending, respectively,[49,51–53] collectively revealing the incorporation of carbonate species in the intermediates. Residual anions from the nickel precursors were also detected, specifically in samples synthesised from $Ni(NO_3)_2$ where a nitrate-related absorption around 1500 cm^{-1}, attributed to asymmetric stretching of NO_3^- is seen,[54,55] whilst intermediates derived from $Ni(OAc)_2$ exhibited characteristic acetate features, including a C–H stretching band at 2977 cm^{-1}, as well as asymmetric and symmetric stretching of COO^- at 1582 and 1375 cm^{-1} respectively.[56]

To further probe the intermediate surface chemistry, XPS was performed, and differences were again observed in the spectra when the precipitating base was changed. The survey spectra, Fig. S1a, confirm C, Ni and O as the main elements present in all samples. The C 1s core level spectra are presented in Fig. 2d, where the signals contain contributions from adventitious carbon, residual acetate from the $Ni(OAc)_2$ precursor, and/or carbonate species introduced by $NaHCO_3$—there are distinct differences observed when the base is varied. For samples precipitated using NaOH, the spectra are dominated by the C–C/C–H component at 284.8 eV, with a weaker O–C═O related peak appearing in the 288.6–288.9 eV region. When $NaHCO_3$ was used a strong peak around 289.5 eV emerges, this component represents an overlapping signal between the O–C═O envelope and carbonate species,[57] its higher binding energy being attributed to the electron-deficient carbonate environment, in which coordination to electronegative oxygen atoms withdrew electron density, increasing effective charge on carbon.[58] Owing to spin–orbit splitting,[59] the Ni 2p core level spectra contain both $2p_{3/2}$ and $2p_{1/2}$ components; however, only the more intense $2p_{3/2}$ region is shown here in Fig. 2e, with peak modelling following the protocol described by Biesinger *et al.*[60,61] A broadened and slightly asymmetric main peak is seen in all samples, with maxima centred at ~855.3–856.3 eV, consistent with reported values for Ni^{2+} in hydroxide and carbonate environments.[62] The line shape is attributed to multiplet splitting, which arises when photoionisation generates a Ni 2p core hole that undergoes exchange interactions with partially occupied Ni 3d orbitals, developing multiple final-state configurations with different energies.[63] Additionally, pronounced shake-up satellite features are observed on the higher binding energy side of the main peak (~860.6–861.5 eV), caused by the outgoing photoelectron exciting a valence electron to a higher unoccupied energy level, commonly seen in transition metal complexes.[59,64] This corresponds to an energy separation of ~5.3 eV from the main peak, within the typical range reported for Ni^{2+} species, and clearly distinguishes the spectra from metallic nickel (Ni^0), which exhibits a lower Ni $2p_{3/2}$ main peak (~852.6 eV) and negligible satellite intensity.[62]

The $2p_{3/2}$ binding energies of Ni^{2+} and Ni^{3+} overlap, thus the assignment of $Ni(OH)_2$ and $Ni_m(OH)_n(CO_3)_p$ as the intermediate species does not discriminate the presence of NiOOH (Ni^{3+}), where the main peak of the $2p_{3/2}$ spectra appears at ~855.8 eV,[62] hence assigning oxidation states based solely on this spectral region may be ambiguous. Therefore, the Ni-LMM Auger spectra were examined to enable more definitive assignment of oxidation state, Fig. S1b. These spectra display a broader envelope, and the additional shoulder on the lower kinetic energy side is absent, characteristic of NiOOH, confirming the predominance of Ni^{2+}.[65] When compared with NaOH precipitated intermediates, the Ni 2p spectra of samples obtained using $NaHCO_3$ show a small negative shift (~1 eV) in the main peak, in line with the carbonate-related trend observed in the C 1s region. Fitting of these spectra also required extra components, containing both $Ni(OH)_2$ and $NiCO_3$-like profiles, indicative of a more complex environment around Ni. This is expected under alkaline carbonate conditions, where precipitates are commonly reported as basic nickel carbonate, typically written as $Ni_m(OH)_n(CO_3)_p$, rather than a neutral nickel carbonate ($NiCO_3$) phase.[66,67] The O 1s core level spectra are shown in Fig. S1c. In the NaOH series, the O 1s peak is centred at 530.7 eV, associated with hydroxyl oxygen (Ni–OH).[68] However, the use of $NaHCO_3$ resulted in a shift of the peak towards higher binding energy together with noticeable broadening, giving rise to a carbonate-related contribution at 531.6 eV with a larger full width at half maximum (FWHM) of 2.2 eV (1.6 eV for the hydroxyl peak in the NaOH intermediates). Taken together, these data indicate that when NaOH is used as the precipitating base, the resulting intermediate is crystalline $Ni(OH)_2$; the morphology of the intermediate is shown to be dependent on the Ni-precursor, with $Ni(NO_3)_2$ yielding flake-like structures and $Ni(OAc)_2$ producing spherical particles. Using $NaHCO_3$ as a precipitating base led to the formation of mixed hydroxide-carbonate intermediates, $Ni_m(OH)_n(CO_3)_p$, that lack long-range crystallographic order and adopt a spherical morphology.

Conversion of the intermediates to NiO_x

Having developed an understanding of the intermediates, we consider their thermal conversion to NiO_x (eqn (2)). Fig. 3 shows the thermal analysis of the four intermediates, combining simultaneous thermogravimetric analysis (TGA) and differential scanning calorimetry (DSC), with derivative thermogravimetric (DTG) curves extracted from the TGA traces to resolve overlapping mass loss events. Despite differences in reaction conditions, all samples followed a three-stage decomposition behaviour. In all cases, the initial heating stage occurs from room temperature to ~200 °C. Comparing the intermediates precipitated using NaOH, those precipitated from $NaHCO_3$ have a significant mass loss in this range, indicating an increased proportion of physisorbed water or –OH in the precipitates, while no structural transformation is observed in any of the samples. For all samples, the greatest mass loss occurs during the second stage of heating, ~200 to 350 °C, which corresponds to NiO_x formation. Over this temperature range, $Ni(OH)_2$ is transformed through dehydration, whereas

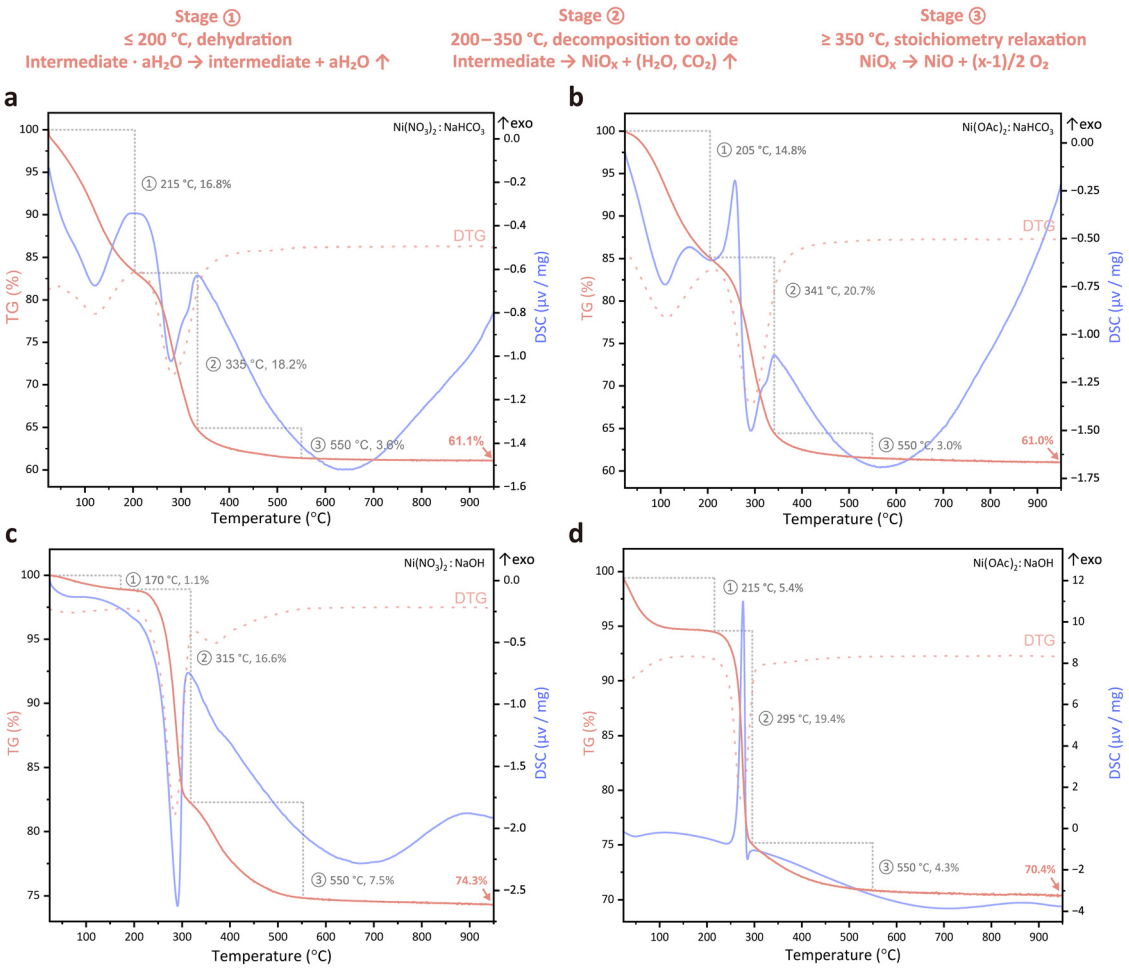

Fig. 3 Thermal analysis of the intermediate powders prepared under four precipitation conditions. TGA (red) and DSC (blue) curves are displayed together with the DTG profiles (dashed red), derived from the corresponding TGA traces. Data shown for (a) $Ni(NO_3)_2$: $NaCO_3$, (b) Ni(OAc) : $NaHCO_3$, (c), $Ni(NO_3)_2$: NaOH and (d) $Ni(OAc)_2$: NaOH. The three main mass-loss stages, dehydration, decomposition to NiO_x, and subsequent stoichiometry relaxation of NiO_x are summarised above.

$Ni_m(OH)_n(CO_3)_p$ decomposes *via* carbonate breakdown, accompanied by the release of carbon dioxide and water. Extending the temperature to ~550 °C, gradual mass loss is observed, attributed to the formation of the more stable oxide species with subtle changes attributed to partial evolution of oxygen in NiO_x toward a more NiO like composition.[69,70] The overall mass loss during heating appears to be governed by the base used for precipitation rather than the Ni source—however differences attributed to the Ni anion can be seen in the DSC data, where an additional exothermic feature is seen during the heating stage of the acetate precursors that may be due to the oxidation of a residual acetate or fragment remaining after washing.[71]

Influence of calcination temperature

Based on the three principal decomposition events identified in the thermal analysis, Fig. 3, the intermediates were calcined at 270, 450, and 650 °C, corresponding to the second and third decomposition stages and to a temperature beyond the third stage, respectively. It should be noted that the thermal analysis data are obtained at a rapid heating rate of 10 °C min^{-1} to amplify the signal. In contrast, for the calcination samples the isothermal treatment enables complete conversion of the intermediates to NiO_x, even at 270 °C, consistent with the literature.[72] XRD and XPS were subsequently used to characterise the products obtained.

Considering first the intermediates annealed at 270 °C, as shown in Fig. 4a, peaks around 37.0, 43.2, 62.7, 75.1, and 79.0° 2θ are observed for all samples, which can be assigned to the (111), (200), (220), (311) and (222) planes of rock salt NiO (ICDD: 04-011-9039), respectively. No diffraction peaks from the intermediates were observed, suggesting their complete degradation and formation of NiO_x. Notable differences in relative peak intensities were observed between samples, particularly between the (111) and (200) diffraction peaks where NiO_x obtained from the $Ni(OAc)_2$: NaOH intermediate showed a dominant (111) peak whilst for all other samples the (200) peak was dominant.

In fcc lattices, such as NiO_x, the close-packed layers stack along the ⟨111⟩ direction, and consequently stacking faults primarily disturb periodicity along this direction.[73] The

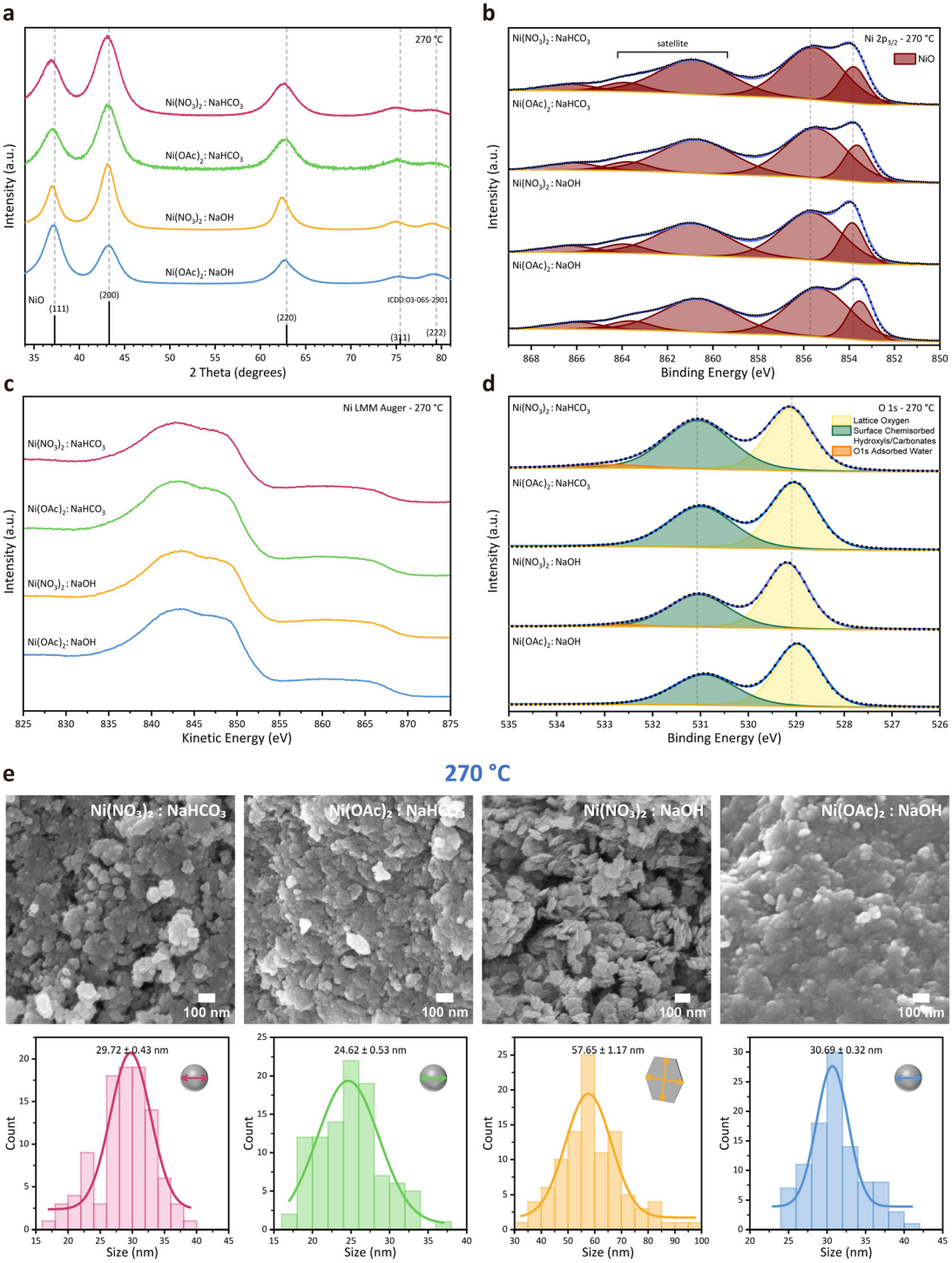

Fig. 4 Characterisation of NiO_x products obtained after calcination at 270 °C, using intermediates prepared by the four precipitation conditions. (a) XRD patterns alongside the reference data of cubic NiO (ICDD: 03-065-2901). XPS spectra for (b) fitted Ni $2p_{3/2}$ core level spectra, (c) Ni LMM Auger spectra, and (d) fitted O 1s core level spectra. (e) SEM and corresponding particle size distributions show the morphology and size. Particle sizes were determined from the dimensions illustrated in the inset of each histogram.

hydroxide intermediate formed from the $Ni(OAc)_2$: NaOH system shows such faults, which may persist after calcination, leading to an enhanced relative intensity of the (111) reflection. Complete conversion to NiO_x is also supported by the XPS data. The survey spectra, in Fig. S2a, show Ni and O, along with a C 1s signal, as anticipated for air-exposed powders. The C 1s core level spectra, in Fig. S2b, were fitted with four components at around 284.8 eV (C–C/C–H), 286.2 eV (C–O), 288.0 eV (C═O), and 288.8 eV (O–C═O), with no appreciable changes observed across the sample set—in common the spectra were dominated

by C–C/C–H contribution, indicating that the carbon signal mainly originated from adventitious surface contamination rather than residual carbonate or acetate species.[74] For the Ni $2p_{3/2}$ region, Fig. 4b, the main peaks and shake-up satellites were located at binding energies characteristic of Ni^{2+} species in NiO, with the overall complex profile arising from the multiplet (exchange) splitting.[60–63] Two peaks at approximately 853.8 and 855.7 eV were resolved in the main peak region after calcination, in contrast to the single feature (~855.3–856.3 eV) observed for the intermediates. A five-component model following the approach of Biesinger *et al.* was then applied to fit the spectra across all final products.[60,61] The Ni LMM Auger spectra, in Fig. 4c, likewise marked this transformation, showing a well resolved two peak structure, rather than the intermediate related broad envelope. Additional insight into the oxygen chemical environment was obtained from the O 1s core level spectra, shown in Fig. 4d. After calcination, the products show a distinct lattice-oxygen component at ~529.1 eV, consistent with Ni–O coordination in the oxide lattice.[75] A higher binding energy feature centred near 531.1 eV was assigned to chemisorbed surface oxygen species, mainly –OH and/or –CO.

To assess the morphology of the NiO_x prepared after calcination, SEM was employed (Fig. 4e). The images show that the morphology of the intermediates is preserved upon calcination at 270 °C. Specifically, the NiO_x prepared from the $Ni(NO_3)_2$: NaOH precursor retained its flake-like morphology, with an average

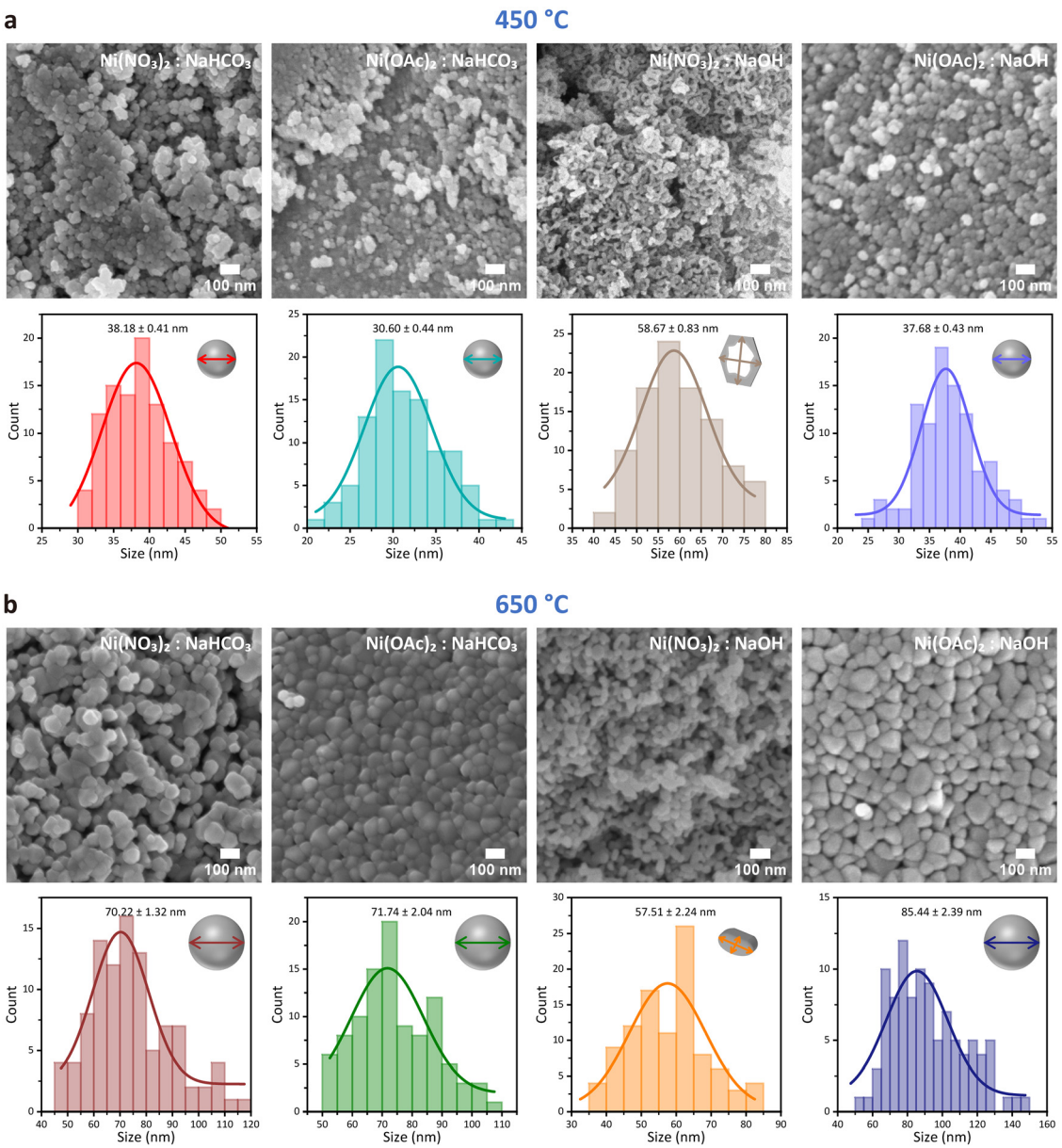

Fig. 5 SEM images and the corresponding particle size distribution of NiO_x products obtained from intermediates prepared *via* the four precipitation conditions shown in the upper captions following calcination at (a) 450 °C and (b) 650 °C. Particle sizes were determined from the dimensions illustrated in the inset of each histogram.

particle size of 57.7 nm, comparable to that of the corresponding intermediate (57.9 nm), whilst all others displayed a spherical morphology, exhibiting a slight increase in mean diameter compared with their intermediates, to 29.7, 24.6 and 30.7 nm for the $Ni(NO_3)_2$: $NaHCO_3$, $Ni(OAc)_2$:$NaHCO_3$ and $Ni(OAc)_2$: NaOH systems, respectively. Transmission electron microscopy (TEM) provided higher resolution images, as shown in Fig. S3. For the $Ni(NO_3)_2$: NaOH product the flake-like morphology is clear, with thin structures having large lateral dimensions; for all other conditions small particles are observed to aggregate together. Thus, we can conclude that 270 °C is a suitable temperature to convert the intermediate phases to NiO_x, and the morphology of the intermediates is preserved in the final product.

Using fresh intermediate samples, the calcination temperature was increased to 450 and 650 °C respectively, again with a 2-hour isothermal hold. The SEM, Fig. 5, and TEM, Fig. S4, images reveal distinct morphological changes in the NiO_x that correlate with the calcination temperature, and it is apparent that the intermediates are directly influencing the properties of the final products. For all samples other than those prepared from the $Ni(NO_3)_2$: NaOH precursor, spherical particles are prepared that experience temperature-driven coarsening, as evidenced by the mean diameter reaching 38.2, 30.6, and 37.7 nm at 450 °C and further increasing to 70.2, 71.7, and 85.4 nm at 650 °C for the $Ni(NO_3)_2$: $NaHCO_3$, $Ni(OAc)_2$:$NaHCO_3$ and $Ni(OAc)_2$: NaOH systems, respectively. To provide a clearer overview of this trend, the particle sizes of all intermediates and calcined NiO_x samples are summarised in Fig. S5, with the corresponding values listed in Table S5. Such coarsening is attributed to the higher atomic mobility at elevated temperatures, which facilitates surface diffusion and interparticle mass transport, enabling larger particles to grow at the expense of smaller ones and thereby reducing the overall surface energy.[76,77] However, unexpected changes were observed for the sample prepared from $Ni(NO_3)_2$: NaOH, where the flake-like structure obtained at 270 °C evolves into a ring-like structure at 450 °C, with an average lateral dimension of 58.7 nm, before transforming into dense, irregularly shaped particles measuring around 57.5 nm at 650 °C.

TEM provided clearer evidence by showing partially preserved ring-like outlines together with broken segments. We relate these morphological changes to the decomposition pathway of the $Ni(OH)_2$ intermediate, suggesting that, as seen in the third stage in the thermal analysis, Fig. 3a, oxygen evolution from non-stoichiometric NiO_x results in porosity developing in the ultrathin flakes, driving the formation of the rings. This is supported by the TGA data, which show a mass loss of around 7.5% in the 315–550 °C temperature window, significantly greater than that observed over the same range with the other precursors. Increasing the calcination temperature to 650 °C results in more gas evolution and the breakdown of the ring-like structure into irregular fragments. Interestingly, even though the $Ni(OAc)_2$: NaOH route involved a hydroxide intermediate and mass loss is observed in the final stage of heating (4.3%), which is greater than seen in the carbonate intermediates, the morphology of the intermediates is preserved on heating. Like the carbonate intermediates we speculate that the spherical form enables gas-evolution, but their isotropic nature does not result in the same gas-evolution porosity, and the intermediate morphology is preserved; however, the anticipated grain growth and coarsening are seen.

The samples precipitated using NaOH exhibit some degree of crystallinity at the intermediate stage whereas those precipitated from the $NaHCO_3$ lack long-range order and when annealed at 270 °C all samples show the onset of crystallinity (Fig. 4a); however, the diffraction peaks are broad, indicative of the small crystallite size and a defect-rich structure.[78] XRD patterns of the intermediates annealed at 450 and 650 °C are shown in Fig. 6a and b. The NiO_x prepared from $Ni(OAc)_2$: NaOH again show a preferred orientation where the (111) peak is the most intense, with all others showing behaviour consistent with the reference powder pattern, with the (200) peak being most intense, and this may indicate that structural order introduced during the precipitation stage is not lost during calcination. Increasing temperature results in a narrowing of the diffraction peaks and an increase in peak intensity, indicating crystallite growth and an increase in overall long-range order, with no additional peaks emerging *i.e.* phase purity is preserved. Analyses of the most intense diffraction peaks ((111) and (200)) are provided in Table S6. All samples show an increase in crystallite size as calcination temperature increases, generally forming small (<5 nm) crystallites at 270 °C, increasing to larger crystallites (>30 nm) at 650 °C, and there are no obvious systematic variations in size observed between samples. The same major diffraction peaks also show a systematic shift to higher 2θ values as calcination temperate increases, and the peak positions at 270 °C differ noticeably from those at higher temperatures, with no appreciable shifts seen at $>$ 450 °C, indicating that a stable structure has been formed.

In addition to the bulk structural characterisation obtained by XRD, XPS was employed to investigate the near-surface structure and bonding, as shown in Fig. S6 and S7. All survey spectra show the presence of C, Ni and O. The C 1s signal, arising primarily from surface carbon contamination, was fitted with four components without obvious peak shifts. Clear temperature-dependent variations were observed in the Ni $2p_{3/2}$ region, with two peaks resolved in the main peak region (852–858 eV) for all samples. At 450 and 650 °C these peaks show a subtle reduction in binding energy compared with the samples calcined at 270 °C, and the lowest binding energy feature increases in relative intensity with increased calcination temperature (Fig. 6c). As the calcination temperature increases, residual solvent and weakly bound surface species *e.g.* hydroxyl groups, organic species, nitrates, acetates, or other species are progressively removed, and would result in a reorganisation of the local environment around Ni. The Ni LMM Auger spectra show similar behaviour where the characteristic double peak line shape at peak maxima of 843–844 eV is observed for all samples, albeit with a subtle shift to higher kinetic energy, as calcination temperature increases, particularly from 270 °C to higher temperatures. Changes in the oxygen environment are also observed in the O 1s core level spectra. Whilst no obvious changes in peak position are seen, the 450 and 650 °C samples

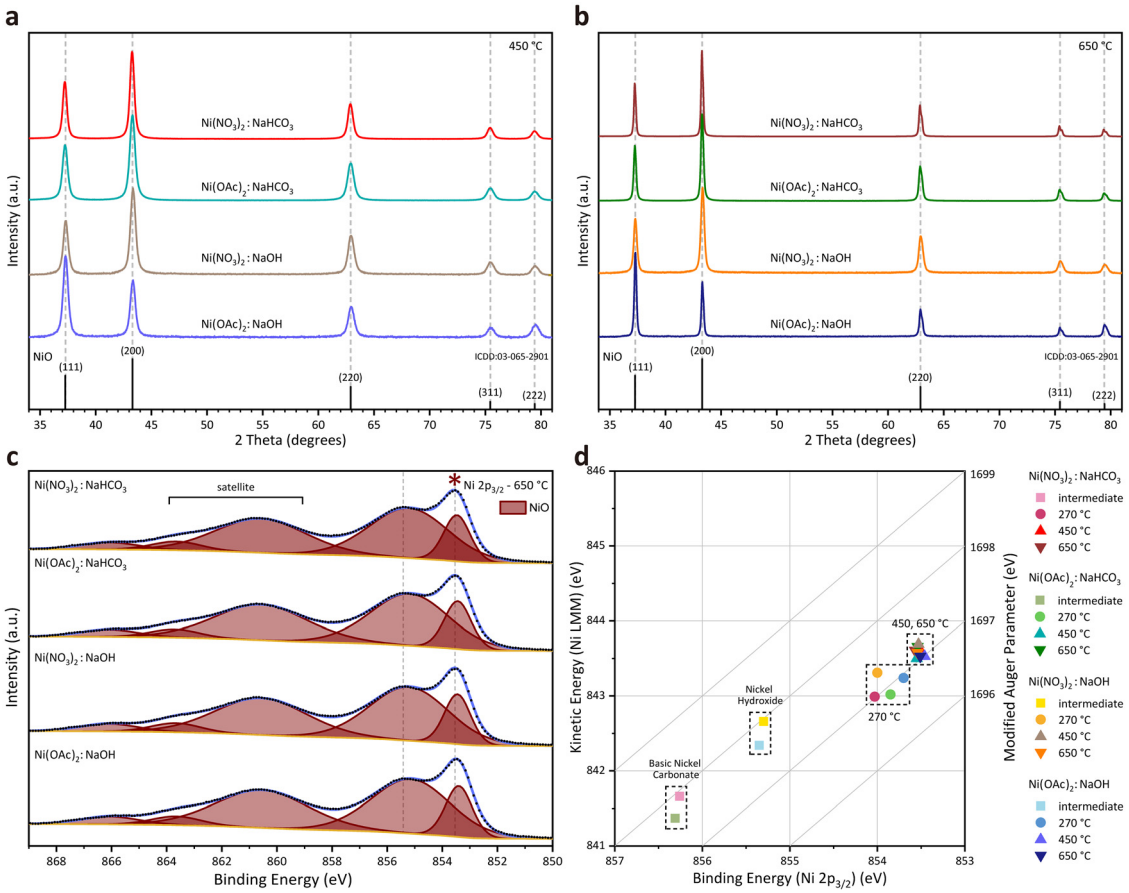

Fig. 6 Influence of calcination temperature on NiO_x products obtained from intermediates prepared under four precipitation conditions. XRD patterns of samples calcined at (a) 450 °C and (b) 650 °C, together with the reference data of cubic NiO (ICDD: 03-065-2901). (c) Ni $2p_{3/2}$ core level XPS spectra of the 650 °C products with peak fitting. The feature marked by an asterisk corresponds to the lowest binding-energy component discussed in the main text. (d) The Ni $2p_{3/2}$–Ni LMM Wagner plot illustrating the variation in the Ni chemical environment from the precipitated intermediates to the calcined NiO_x products at different temperatures. The calculated Auger parameter values are provided in Table S7.

show variations in the relative intensities of the lattice and surface oxygen peaks compared with the samples calcined at 270 °C, with a reduction in surface species seen at higher temperature, further supporting the removal of weakly bound groups.

Given the strong spectral overlap of the intermediate and NiO_x, Wagner plot analysis was carried out, where the modified Auger parameter was employed to resolve the Ni local environment. Using the peak positions of the Ni $2p_{3/2}$ and Ni LMM features, an Auger parameter around 1697.5 eV was identified as a practical boundary (Fig. 6d). The data show that all the intermediates lie above this value, whilst all NiO_x products lie below it, highlighting a clear phase distinction. Within this framework, the intermediate samples can be further separated into two regions, corresponding to $Ni(OH)_2$ and amorphous $Ni_m(OH)_n(CO_3)_p$. Considering the NiO_x samples, the data show that those prepared at 450 and 650 °C cluster closely together, whilst there is a subtle offset for the 270 °C samples. Collectively, XPS reveals more distinct differences in surface chemistry between samples calcined at 270 and 450 °C, whereas the 450 and 650 °C samples were largely similar, which reinforces the XRD analyses and supports the formation of a stable oxide at > 450 °C.

Properties of the morphology-controlled NiO_x

The specific surface areas of all species prepared were determined using the Brunauer–Emmett–Teller (BET) method from nitrogen sorption measurements,[79] as shown in Fig. 7a, b and Table S8. In general, all samples exhibited similar adsorption–desorption isotherms, characterised by a gradual nitrogen uptake at low relative pressures, followed by a much steeper increase at higher relative pressures, with hysteresis observed during desorption, as shown in Fig. S8. This behaviour is associated with the capillary condensation within mesoporous voids formed between agglomerates, which are composed of loosely coherent assemblies of nanoparticles.[80,81] Among the spherical products prepared at the same temperature, differences in BET surface area are observed, with the largest variation found at 270 °C. The $NaHCO_3$ derived NiO_x displays higher specific areas of 206.8 and 247.3 m^2g^{-1} for the $Ni(NO_3)_2$ and $Ni(OAc)_2$ systems, respectively, compared with 162.8 m^2g^{-1} for the $Ni(OAc)_2$: NaOH system. Consistent with this, SEM images

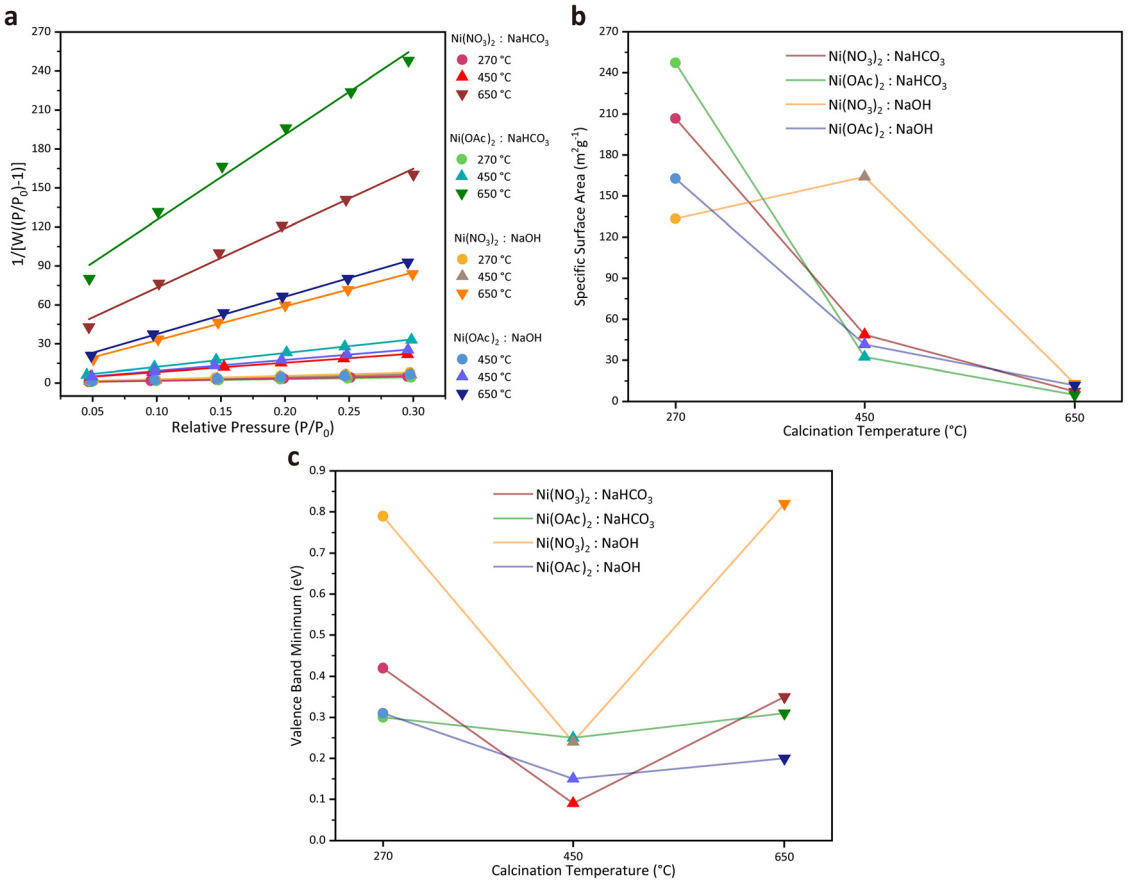

Fig. 7 (a) Brunauer–Emmett–Teller (BET) plots obtained from the nitrogen adsorption isotherms over the relative pressure range of $0.05 < P/P_0 < 0.30$, with linear fitting used for surface area determination. (b) Summary of the BET specific surface areas of all NiO_x products as a function of calcination temperature. (c) Summary of the valence band minimum (VBM) values of all NiO_x products as a function of calcination temperature.

of samples calcined at 270 °C reveal correspondingly smaller particle sizes for the $NaHCO_3$ derived products. Calcination temperature had the most pronounced effect on specific surface area, which decreased significantly with increasing temperature, again consistent with the SEM and XRD data. There is a notable difference in the behaviour of the $Ni(NO_3)_2$: NaOH system that is attributed to the observed morphological evolution. As the flake-like morphology formed at 270 °C transforms into nanorings when calcined at 450 °C, with an accompanying surface area increase from 133.4 to 164.0 m^2g^{-1}. Further calcination at 650 °C causes fragmentation of the nanorings together with particle coarsening, reducing the surface area to 13.0 m^2g^{-1}, again in agreement with the general behaviour observed at higher calcination temperatures.

The valence band maximum (VBM) relative to the Fermi level (E_F) was determined from valence band XPS spectra, as shown in Fig. 7c and S9. This measures the occupied electronic states closest to the E_F, rather than the chemically specific core levels typically examined in conventional XPS. The spectra show a strong dependence of the electronic structure on calcination temperature and synthesis route. All samples exhibited VBMs close to the E_F, consistent with p-type NiO_x. The smallest VBM-E_F separations, ranging from 0.09 to 0.25 eV, were observed after calcination at 450 °C, indicating an enhanced p-type characteristic. This behaviour is consistent with an increased concentration of acceptor-type defects, such as Ni^{3+} and nickel vacancies, that promote hole conductivity.[11,14] At 270 °C, the generally larger separations likely reflect insufficient thermal energy to promote oxidation of Ni^{2+} to Ni^{3+} during conversion of the hydroxide/carbonate intermediates to NiO_x. Further increasing the temperature to 650 °C shifted the VBM away from E_F for most samples, consistent with stoichiometric relaxation and a reduced defect-mediated p-type characteristic. The magnitude of these changes depended strongly on the precursor chemistry as well, with nitrate derived samples, particularly $Ni(NO_3)_2$: NaOH, showing the greatest temperature sensitivity, whereas acetate derived samples exhibited more stable VBM positions.

To further demonstrate the practical relevance of the NiO_x developed in this work, representative products prepared from the $Ni(NO_3)_2$: NaOH (270 and 450 °C) and $Ni(NO_3)_2$: $NaHCO_3$ (270 and 650 °C) routes were applied as surface modifiers on bismuth vanadate ($BiVO_4$) photoanodes for water splitting. As a p-type semiconductor, NiO_x can act as a surface modifier that facilitates interfacial hole extraction and mitigates surface recombination in $BiVO_4$ photoanodes, making it a promising material for photoelectrochemical (PEC) applications.[82,83] Chopped-light chronoamperometry (CA), which monitors the

photocurrent response under periodic light-on/off cycles, was therefore employed to evaluate how the synthesis-derived NiO_x morphologies influence the PEC response. Compared with pristine $BiVO_4$, all NiO_x-modified photoanodes exhibit improved PEC performance, as shown in Fig. 8. The current density increases from approximately 0.14 mA cm^{-2} for bare $BiVO_4$ to 0.36, 0.37, 0.43 and 0.62 mA cm^{-2} for the flake-like, large spherical, ring-like and small spherical samples, respectively, corresponding to enhancements around 2.5-, 2.6-, 3.0- and 4.4-fold. From a morphological perspective, the observed trend can be understood by considering how the deposited NiO_x particles construct the $BiVO_4$/NiO_x/electrolyte interface. An effective surface modifier should provide sufficient contact with the electrode while maintaining a large electrolyte-accessible surface area.[84] Within the $Ni(NO_3)_2$: NaOH series, the ring-like morphology gives a higher photocurrent than the flake-like counterpart, consistent with its more open architecture and higher BET surface area. A similar trend is observed for the spherical morphologies prepared from the $Ni(NO_3)_2$: $NaHCO_3$ system, where particle coarsening after high-temperature calcination leads to a reduction in surface area and consequently lower photocurrent. Notably, the small spherical NiO_x exhibits the highest current density among all the morphologies investigated. In addition to its high surface area, the three-dimensional small spherical morphology is likely to maintain a more uniform particle distribution during spray deposition, whereas the two-dimensional flakes are more prone to overlap and aggregate,[85,86] thereby reducing the number of productive $BiVO_4$/NiO_x/electrolyte contact regions. Although the overall PEC response also depends on crystallinity, defect chemistry and electronic structure,[87,88] all of which likewise evolve with the synthesis conditions, the observed trends here highlight the role of NiO_x morphology, through variations in both particle shape and size, in tuning its function as a $BiVO_4$ surface modifier.

Conclusions

We have systematically investigated the influence of base type, nickel source, and calcination temperature on the synthesis of NiO_x nanomaterials prepared *via* a chemical precipitation route. Both precipitated intermediates and final products underwent extensive morphological, crystallographic and compositional analysis. We show that the composition of the intermediates is primarily determined by the choice of base, where NaOH yields crystalline $Ni(OH)_2$ and $NaHCO_3$ produces amorphous $Ni_m(OH)_n(CO_3)_p$. At the same time, the nitrate and acetate anions of the nickel precursors modify the precipitation environment through their different coordination behaviours, further dictating the characteristics of the resulting materials. More importantly, we found that the nature of the intermediate plays an essential role in determining the morphology of the final NiO_x. Under relatively mild calcination conditions, the

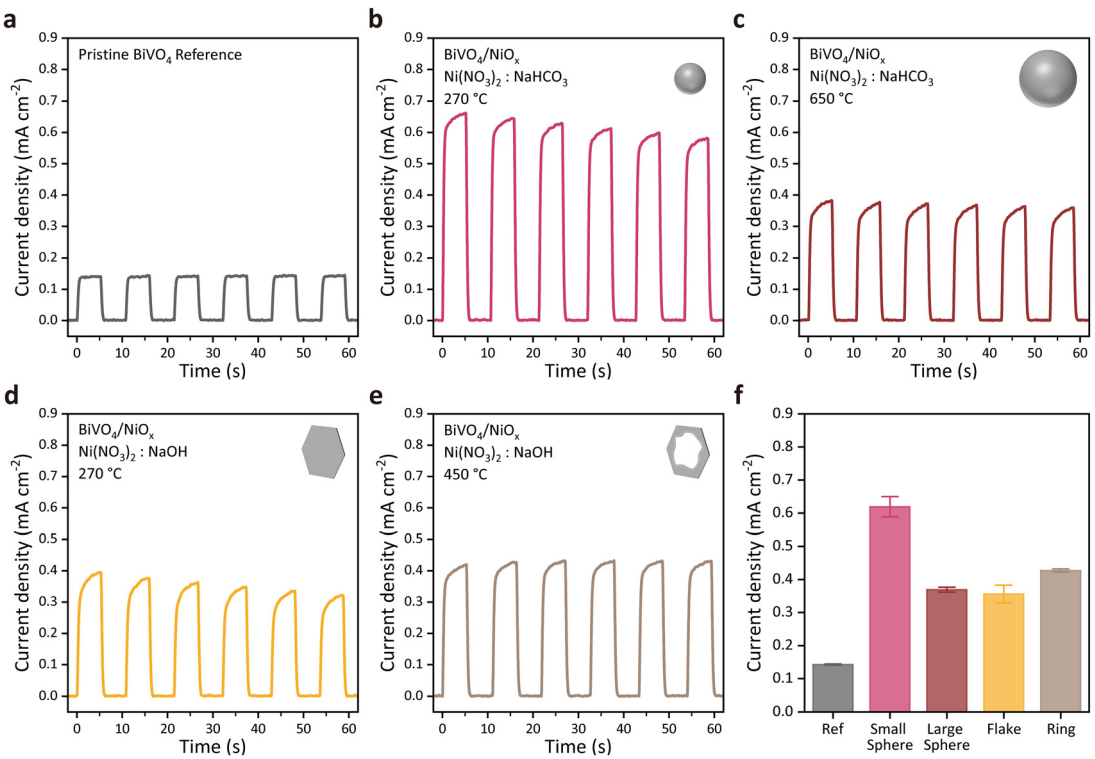

Fig. 8 Photoelectrochemical (PEC) performance of the morphology-controlled NiO_x developed in this work. Chopped-light chronoamperometry (CA) measurement of (a) pristine $BiVO_4$ and $BiVO_4$ photoanodes modified with NiO_x prepared from the $Ni(NO_3)_2$: $NaHCO_3$ precursor system following calcination at (b) 270 and (c) 650 °C, and from the $Ni(NO_3)_2$: NaOH precursor system following calcination at (d) 270 and (e) 450 °C. The corresponding NiO_x morphologies are shown as the insets. (f) Comparison of the photocurrent densities for the pristine and modified $BiVO_4$ photoanodes. Error bars represent the standard deviation calculated from the individual light-on cycles.

oxide products largely inherit the morphology of their intermediate, whereas higher temperature calcination promotes crystal growth and, in some cases, substantial morphological evolution. A notable example is the $Ni(NO_3)_2$: NaOH system, in which the unique flake-like morphology observed in the intermediate phase is retained after calcination at 270 °C, and evolves into a ring-like structure at 450 °C that subsequently fragments at 650 °C. In contrast, all other intermediates and oxide products exhibit a spherical morphology that increases in size and crystallinity with increased annealing temperature. Structural features established during precipitation are also preserved during calcination, as evidenced by the preferred orientation observed for the $Ni(OAc)_2$: NaOH system across all calcination temperatures. Whilst morphological and compositional differences are observed in the intermediate species, Ni^{2+} is however dominant in all intermediates. Similarly, when the calcination temperature is varied, Ni^{2+}, and thus NiO_x, is confirmed at all temperatures with a subtle structural relaxation seen between 270 and 450 °C. By linking precursor chemistry, intermediate-phase formation, and decomposition pathway during calcination to the characteristics of the final NiO_x products, our work provides new insights into the mechanism of morphology evolution. These distinct morphologies also exhibit different structural, surface, electronic and photoelectrochemical properties, highlighting the significance of morphology control for material functionality. Our results establish how simple synthetic variables can be used to control NiO_x phase evolution and morphology, offering practical design principles for the synthesis of nanoscale NiO_x and other metal oxide nanomaterials.

Materials and methods

Synthesis of NiO_x nanomaterials

A chemical precipitation route adopted from previous work was used to synthesis the NiO_x nanomaterials in this study.[72] The precipitation conditions were systematically varied by pairwise combinations of two nickel salts with two bases, resulting in four distinct conditions as listed in Table S1.

In a typical procedure, a 1.0 M Ni^{2+} precursor solution was prepared by dissolving 4 mmol of nickel salt, either nickel(II) nitrate hexahydrate ($Ni(NO_3)_2{\cdot}6H_2O$, 94.5–105.5% by EDTA titration, Sigma-Aldrich) or nickel(II) acetate tetrahydrate ($Ni(OAc)_2{\cdot}4H_2O$, 98%, Sigma-Aldrich), in 4 mL of deionized water under stirring at room temperature. Aqueous solutions of sodium hydroxide (NaOH, 98%, Sigma-Aldrich) and sodium bicarbonate ($NaHCO_3$, 99%, Thermo Fisher Scientific) were prepared at concentrations of 10 M and 1 M, respectively. To ensure consistent stoichiometric control across all samples, the base amount was determined by the targeted intermediate. Specifically, 8 mmol NaOH was used to achieve an OH^-/Ni^{2+} ratio of 2, favouring the formation of nickel hydroxide ($Ni(OH)_2$). In contrast, carbonate-based intermediates ($Ni_m(OH)_n(CO_3)_p$) were obtained by applying 4 mmol of $NaHCO_3$, corresponding to an HCO_3^-/Ni^{2+} ratio of 1. The base solution was introduced into the nickel precursor in a single addition at room temperature, leading to immediate precipitation, and the suspension was stirred for an additional 20 min. The precipitate was subsequently collected by centrifugation at 5000 rpm for 3 min, washed with three cycles of deionized water, and dried in an oven at 70 °C overnight. Following grinding to a fine powder, the intermediates were calcined in a tube furnace under air at 270, 450 and 650 °C for 2 h, yielding black NiO_x products.

Materials characterisation

Fourier transform infrared (FTIR) spectra were recorded using an Agilent Cary 630 spectrometer equipped with an attenuated total reflectance (ATR) module, over the range of 4000–400 cm^{-1}.

X-ray photoelectron spectroscopy (XPS) data were acquired on a Thermo Fisher K-Alpha$^+$ system, employing a monochromatic Al Kα source ($h\nu$ = 1486.6 eV) with a 400 μm beam spot. Survey scans together with high-resolution core-level spectra of C 1s, Ni 2p and O1s, as well as Ni LMM Auger and valence band spectra, were captured. Spectral fitting was carried out in KherveFitting,[89] and binding energies were calibrated against the C–C component of the C 1s peak at 284.8 eV.

X-ray diffraction (XRD) patterns were measured on a Malvern PANalytical Empyrean diffractometer using Cu Kα radiation (λ = 1.5406 Å) at 40 kV and 40 mA. Data were collected with a step size of 0.03° over 2θ ranges of 15–65° for intermediates, and 34–81° for NiO_x, followed by phase analysis in HighScore.

Thermogravimetric analysis (TGA) and *differential scanning calorimetry (DSC)* were conducted on a Netzsch STA 449C F5 Jupiter simultaneous thermal analyser. Measurements were performed in air at a flow rate of 60 mL min^{-1} from 25 to 950 °C with a heating rate of 10 °C min^{-1}. Derivative thermogravimetric (DTG) curves were derived from the TGA data using Origin.

Scanning electron microscopy (SEM) imaging was carried out on a Zeiss Auriga CrossBeam FIB-SEM, operated at an accelerating voltage of 5 kV. Samples were mounted on conductive carbon tape and coated with a 20 nm chromium layer. The particle size analysis was performed from SEM images using ImageJ. Depending on the particle morphology, either the particle diameter or the lateral flake dimensions were measured, as illustrated in the corresponding figure inset. For each sample, at least 100 particles were analysed to obtain the size distribution, and the mean value was determined by Gaussian fitting of the resulting histogram.

Transmission electron microscopy (TEM) was performed using a JEOL 2100 Plus operated at 200 kV. Powders were dispersed in deionized water (10 mg mL^{-1}), sonicated for 5 min, and deposited onto holey carbon-coated copper grids.

Nitrogen sorption isotherms were obtained at 77 K using a Quantachrome Autosorb iQ surface area analyser. Prior to analysis, samples were degassed under vacuum at 100 °C for 12 h to remove physically adsorbed moisture and other species from the sample surface. The acquired data were processed using Quantachrome TouchWin software, from which the specific surface area was determined according to the BET method.[79,80]

Photoelectrochemical (PEC) measurements were conducted using bismuth vanadate ($BiVO_4$) photoanodes fabricated by aerosol-assisted chemical vapour deposition (AA-CVD) on

fluorine-doped tin oxide (FTO) substrates, following our previously reported procedure.[90] For NiO_x modification, the powders were deposited onto the $BiVO_4$ surface by spray coating. Briefly, 50 mg NiO_x was dispersed in a mixture of isopropanol (99.5%, Sigma-Aldrich, 2 mL) and ethanol (99.8%, Sigma-Aldrich, 2 mL), followed by the addition of 1 mL of 0.25 wt% naphthol (99%, Sigma-Aldrich) in ethanol. After ultrasonication for 5 min, the resulting suspension was spray coated onto $BiVO_4$ photoanodes maintained at 80 °C and subsequently dried in an oven at 80 °C for 8 h. The electrode was then characterized by chopped-light chronoamperometry (CA) in a custom-built three-electrode cell, using a pristine $BiVO_4$ or NiO_x modified $BiVO_4$ photoanode as the working electrode, a Pt mesh as the counter electrode, and an Ag/AgCl electrode as the reference electrode. All measurements were performed in 0.5 M Na_2SO_4 electrolyte at an applied potential of 1.23 V_{RHE}, with the exposed electrode area defined by a circular aperture. Illumination was provided through the FTO substrate using a continuous-wave 405 nm laser (spot diameter ~0.3 mm), while a mechanical shutter periodically interrupted the incident beam to generate chopped-light CA traces. The photocurrent response was recorded as a function of time under repeated light/dark cycles and converted to current density based on the illuminated spot area.

Conflicts of interest

There are no conflicts to declare.

Data availability

The data supporting the findings of this study are available in the supplementary information (SI) accompanying this article. Additional data requests can be made to the corresponding author upon reasonable request.

Supplementary information is available. See DOI: https://doi.org/10.1039/d6tc01477a.

Acknowledgements

Longren Li acknowledges Imperial College London for a President's PhD Scholarship.

References

1 C. Liang, S. Wang, S. Sha, S. Lv, G. Wang, B. Wang, Q. Li, J. Yu, X. Xu and L. Zhang, *J. Mater. Chem. C*, 2023, **11**, 4288–4317.
2 Y. G. Hwang, V. Nulu, A. Nulu and K. Y. Sohn, *RSC Adv.*, 2023, **13**, 22007–22016.
3 E. Navarrete, C. Bittencourt, P. Umek and E. Llobet, *J. Mater. Chem. C*, 2018, **6**, 5181–5192.
4 M. Khashaei, L. Kafi-Ahmadi, S. Khademinia, A. Poursattar Marjani and E. Nozad, *Sci. Rep.*, 2022, **12**, 8585.
5 N. Tiwari, H. A. Dewi, E. Erdenebileg, R. N. Chauhan, N. Mathews, S. G. Mhaisalkar and A. Bruno, *Sol. RRL*, 2022, **6**, 2100700.
6 F. Bermúdez-Mendoza, D. J. Ramos-Ramos, M. Taeño, G. C. Vásquez, D. Maestre, F. Domínguez-Adame, B. Méndez, R. Martínez-Casado and E. Díaz, *APL Mater.*, 2025, **13**, 091115.
7 D. Zhang, X. Xiong, S. Kang, Z. Meng, F. You, D. Zhao, C. Ding and G. Zeng, *J. Mater. Chem. C*, 2025, **13**, 17313–17323.
8 R. Thundiyil, P. Poornesh, K. Ozga and J. Jedryka, *RSC Adv.*, 2024, **14**, 30011–30036.
9 F. Ma, Y. Zhao, J. Li, X. Zhang, H. Gu and J. You, *J. Energy Chem.*, 2021, **52**, 393–411.
10 W. Ahmad, S. Chandra Bhatt, M. Verma, V. Kumar and H. Kim, *Environ. Nanotechnol., Monit. Manage.*, 2022, **18**, 100674.
11 W.-B. Zhang, N. Yu, W.-Y. Yu and B.-Y. Tang, *Eur. Phys. J. B*, 2008, **64**, 153–158.
12 Y. Gong, S. Zhang, H. Gao, Z. Ma, S. Hu and Z. Tan, *Sustainable Energy Fuels*, 2020, **4**, 4415–4458.
13 K. P. Makhado, M. M. Mphahlele-Makgwane, N. Kumar, P. G. L. Baker and P. R. Makgwane, *Mater. Today Sustainability*, 2024, **25**, 100664.
14 R. Poulain, G. Lumbeeck, J. Hunka, J. Proost, H. Savolainen, H. Idrissi, D. Schryvers, N. Gauquelin and A. Klein, *ACS Appl. Electron. Mater.*, 2022, **4**, 2718–2728.
15 H. Chen and J. H. Harding, *Phys. Rev. B: Condens. Matter Mater. Phys.*, 2012, **85**, 115127.
16 K. Zhu, S. K. Frehan, A. M. Jaros, D. B. O'Neill, J. P. Korterik, K. Wenderich, G. Mul and A. Huijser, *J. Phys. Chem. C*, 2021, **125**, 16049–16058.
17 R. Karsthof, Y. K. Frodason, A. Galeckas, P. M. Weiser, V. Zviagin and M. Grundmann, *Adv. Photonics Res.*, 2022, **3**, 2200138.
18 R. Fukuma, M. Harada, W. Zhao, M. Sawamura, Y. Noda, M. Nakayama, M. Goto, D. Kan, Y. Shimakawa, M. Yonemura, N. Ikeda, R. Watanuki, H. L. Andersen, A. M. D'Angelo, N. Sharma, J. Park, H. R. Byon, S. Fukuyama, Z. Han, H. Fukumitsu, M. Schulz-Dobrick, K. Yamanaka, H. Yamagishi, T. Ohta and N. Yabuuchi, *ACS Cent. Sci.*, 2022, **8**, 775–794.
19 W. Chen, Y. Wu, J. Fan, A. B. Djurišić, F. Liu, H. W. Tam, A. Ng, C. Surya, W. K. Chan, D. Wang and Z. B. He, *Adv. Energy Mater.*, 2018, **8**, 1703519.
20 T. Nathan, A. Aziz, A. F. Noor and S. R. S. Prabaharan, *J. Solid State Electrochem.*, 2008, **12**, 1003–1009.
21 C. Moya, J. Ara, A. Labarta and X. Batlle, *Magnetism*, 2024, **4**, 252–280.
22 M. Imran Din and A. Rani, *Int. J. Anal. Chem.*, 2016, **2016**, 3512145.
23 B. Cardoso, G. Nobrega, I. S. Afonso, J. E. Ribeiro and R. A. Lima, *J. Environ. Chem. Eng.*, 2025, **13**, 116921.
24 A. Rahman and G. Guisbiers, *Metals*, 2024, **14**, 224.
25 J. Joy, A. Krishnamoorthy, A. Tanna, V. Kamathe, R. Nagar and S. Srinivasan, *Appl. Sci.*, 2022, **12**, 9312.
26 S. S. Narender, V. V. S. Varma, C. S. Srikar, J. Ruchitha, P. A. Varma and B. V. S. Praveen, *Chem. Eng. Technol.*, 2022, **45**, 397–409.

27 J. Sukumaran, M. Priya, R. Venkatesan, K. Sathiasivan, M. R. Khan and S. Kim, *Microsc. Res. Tech.*, 2025, **88**, 2830–2842.
28 S. Safa, R. Hejazi, M. Rabbani and R. Azimirad, *Desalin. Water Treat.*, 2016, **57**, 21982–21989.
29 R. Miao, W. Zeng and Q. Gao, *Appl. Surf. Sci.*, 2016, **384**, 304–310.
30 Ö. Kesmez, T. Kuruca, E. Odabaş, N. Cihanoğlu, E. Akarsu and F. Demir, *ChemistrySelect*, 2025, **10**, 1–8.
31 S. Minisha, J. Johnson, S. Mohammad Wabaidur, J. K. Gupta, S. Aftab, M. R. Siddiqui and W.-C. Lai, *Sustainability*, 2023, **15**, 14552.
32 H. M. Hamzah, N. B. Soin, Y. A. Wahab, Md. J. Hossen, M. E. M. Soudagar, M. Nur-E-Alam, M. A. Islam, C. Xu and M. Patel, *Sci. Rep.*, 2025, **15**, 34775.
33 W. M. Haynes, D. R. Lide and T. J. Bruno, *CRC Handbook of Chemistry and Physics: A Ready-Reference Book of Chemical and Physical Data*, CRC Press, Taylor & Francis Group, 2013.
34 S. Romano, S. Trespi, R. Achermann, G. Battaglia, A. Raponi, D. Marchisio, M. Mazzotti, G. Micale and A. Cipollina, *Cryst. Growth Des.*, 2023, **23**, 6491–6505.
35 V. K. LaMer and R. H. Dinegar, *J. Am. Chem. Soc.*, 1950, **72**, 4847–4854.
36 H. You and J. Fang, *Nano Today*, 2016, **11**, 145–167.
37 D. S. Hall, D. J. Lockwood, C. Bock and B. R. MacDougall, *Proc. R. Soc. A*, 2015, **471**, 20140792.
38 T. N. Ramesh and P. V. Kamath, *J. Power Sources*, 2006, **156**, 655–661.
39 M. Toufani, H. Besic, W. Tong and P. Farràs, *Results Chem.*, 2023, **6**, 101031.
40 K. Lawson, S. P. Wallbridge, A. E. Catling, C. A. Kirk and S. E. Dann, *J. Mater. Chem. A*, 2023, **11**, 789–799.
41 D. D. Perrin, *Dissociation Constants of Inorganic Acids and Bases in Aqueous Solution*, Butterworths, 1969.
42 M. T. Weller, J. Rourke, F. A. Armstrong, S. Lancaster and T. Overton, *Inorganic Chemistry*, Oxford University Press, 2025.
43 Y. Yang, F. Liang, M. Li, T. E. Rufford, W. Zhou and Z. Zhu, *ChemSusChem*, 2015, **8**, 2193–2197.
44 H. Liu, P. Wang, X. Qi, J. Liu, A. Yin, Y. Wang, Y. Ye, J. Luo, Z. Ren, S. Yu and J. Wei, *J. Electroanal. Chem.*, 2023, **949**, 117856.
45 M. S. Vidhya, G. Ravi, R. Yuvakkumar, D. Velauthapillai, M. Thambidurai, C. Dang and B. Saravanakumar, *RSC Adv.*, 2020, **10**, 19410–19418.
46 G. S. Gund, D. P. Dubal, S. B. Jambure, S. S. Shinde and C. D. Lokhande, *J. Mater. Chem. A*, 2013, **1**, 4793.
47 W. Ma, J. Xue and H. Cui, *Ionics*, 2016, **22**, 573–579.
48 X. Yi, H. Sun, N. Robertson and C. Kirk, *Sustainable Energy Fuels*, 2021, **5**, 5236–5246.
49 T. Shahid, M. Arfan, A. Zeb, T. BiBi and T. M. Khan, *Nanomater. Nanotechnol.*, 2018, **8**, 1847980418761775.
50 W. Cai, R. Chen, Y. Yang, M. Yi and L. Xiang, *Crystals*, 2018, **8**, 19.
51 C. Rincke, S. Bette, R. E. Dinnebier and W. Voigt, *Eur. J. Inorg. Chem.*, 2015, 5913–5920.
52 C. Matei, D. Berger, A. Dumbrava, M. D. Radu and E. Gheorghe, *J. Sol–Gel Sci. Technol.*, 2020, **93**, 315–323.
53 L. Bai, L. Chen, M. Wu, K. Song, X. Zhou, J. Guo, H. Pan, S. Liu and J. He, *New J. Chem.*, 2023, **47**, 8111–8121.
54 S. He, L. Zhang, S. He, L. Mo, X. Zheng, H. Wang and Y. Luo, *J. Nanomater.*, 2015, **2015**, 1–8.
55 N. Gupta, A. Kumar, S. K. Dhawan, H. Dhasmana, A. Kumar, V. Kumar, A. Verma and V. K. Jain, *Mater. Today: Proc.*, 2020, **32**, 463–467.
56 M. Taibi, S. Ammar, N. Jouini, F. Fiévet, P. Molinié and M. Drillon, *J. Mater. Chem.*, 2002, **12**, 3238–3244.
57 M. C. Biesinger, *Appl. Surf. Sci.*, 2022, **597**, 153681.
58 P. S. Bagus, C. J. Nelin and C. R. Brundle, *J. Vac. Sci. Technol., A*, 2023, **41**, 068501.
59 M. A. Brisk and A. D. Baker, *J. Electron Spectrosc. Relat. Phenom.*, 1975, **7**, 197–213.
60 M. C. Biesinger, B. P. Payne, A. P. Grosvenor, L. W. M. Lau, A. R. Gerson and R. S. C. Smart, *Appl. Surf. Sci.*, 2011, **257**, 2717–2730.
61 M. C. Biesinger, B. P. Payne, L. W. M. Lau, A. Gerson and R. S. C. Smart, *Surf. Interface Anal.*, 2009, **41**, 324–332.
62 A. P. Grosvenor, M. C. Biesinger, R. S. C. Smart and N. S. McIntyre, *Surf. Sci.*, 2006, **600**, 1771–1779.
63 M. A. Isaacs, A. Graf and D. J. Morgan, *Surf. Interface Anal.*, 2025, **57**, 285–290.
64 F. de Groot and A. Kotani, *Core Level Spectroscopy of Solids*, CRC Press, 2008.
65 M. C. Biesinger, L. W. M. Lau, A. R. Gerson and R. S. C. Smart, *Phys. Chem. Chem. Phys.*, 2012, **14**, 2434.
66 A. Packter and S. C. Uppaladinni, *Krist. Tech.*, 1975, **10**, 985–994.
67 M. A. Rhamdhani, E. Jak and P. C. Hayes, *Metall. Mater. Trans. B*, 2008, **39**, 218–233.
68 A. N. Mansour, *Surf. Sci. Spectra*, 1994, **3**, 239–246.
69 D. Wang, R. Xu, X. Wang and Y. Li, *Nanotechnology*, 2006, **17**, 979–983.
70 N. Spinner and W. E. Mustain, *Electrochim. Acta*, 2011, **56**, 5656–5666.
71 J. Hong, G. Guo and K. Zhang, *J. Anal. Appl. Pyrolysis*, 2006, **77**, 111–115.
72 H. Chen, S. Teale, B. Chen, Y. Hou, L. Grater, T. Zhu, K. Bertens, S. M. Park, H. R. Atapattu, Y. Gao, M. Wei, A. K. Johnston, Q. Zhou, K. Xu, D. Yu, C. Han, T. Cui, E. H. Jung, C. Zhou, W. Zhou, A. H. Proppe, S. Hoogland, F. Laquai, T. Filleter, K. R. Graham, Z. Ning and E. H. Sargent, *Nat. Photonics*, 2022, **16**, 352–358.
73 L. Velterop, R. Delhez, Th. H. de Keijser, E. J. Mittemeijer and D. Reefman, *J. Appl. Crystallogr.*, 2000, **33**, 296–306.
74 T. R. Gengenbach, G. H. Major, M. R. Linford and C. D. Easton, *J. Vac. Sci. Technol., A*, 2021, **39**, 013204.
75 G. Pagot, M. Benedet, C. Maccato, D. Barreca and V. Di Noto, *Surf. Sci. Spectra*, 2023, **30**, 024028.
76 F. Wakai, M. Yoshida, Y. Shinoda and T. Akatsu, *Acta Mater.*, 2005, **53**, 1361–1371.
77 J. Lee, J. Jeong, H. Lee, J. Park, J. Jang and H. Jeong, *Crystals*, 2023, **13**, 1311.

78 G. K. Williamson and W. H. Hall, *Acta Metall.*, 1953, **1**, 22–31.
79 M. Thommes, K. Kaneko, A. V. Neimark, J. P. Olivier, F. Rodriguez-Reinoso, J. Rouquerol and K. S. W. Sing, *Pure Appl. Chem.*, 2015, **87**, 1051–1069.
80 K. S. W. Sing, *Pure Appl. Chem.*, 1985, **57**, 603–619.
81 T. Montoya, A. Amrollahi, G. Vitale, N. Hosseinpour and N. N. Nassar, *ACS Appl. Nano Mater.*, 2020, **3**, 5311–5326.
82 M. Zhang, R. P. Antony, S. Y. Chiam, F. F. Abdi and L. H. Wong, *ChemSusChem*, 2019, **12**, 2022–2028.
83 Q. Huang, Y. Qiu, H. Luo, Y. Yuan, X. Li, Z. Wang and W. Mai, *Mater. Lett.*, 2019, **249**, 128–131.
84 J.-Y. Cui, S.-S. Zhu, Y. Zou, Y. Zhang, S.-Y. Yuan, T.-T. Li, S.-Y. Guo, H. Liu and J.-J. Wang, *Catalysts*, 2022, **12**, 1456.
85 L. Tian, F. Xu, G. Sastre, A. Primo, J. Yu and H. García, *Chem. Soc. Rev.*, 2026, **55**, 4244–4302.
86 J. E. ten Elshof, H. Yuan and P. Gonzalez Rodriguez, *Adv. Energy Mater.*, 2016, **6**, 1600355.
87 C.-H. Zhang, Y.-F. Yang, X.-Z. Yue and S.-S. Yi, *Mater. Today Chem.*, 2025, **50**, 103140.
88 S. Manna, A. K. Satpati, C. N. Patra and A. K. Tyagi, *ACS Omega*, 2024, **9**, 6128–6146.
89 G. Kerherve, W. S. J. Skinner, J. A. Hochhaus, A. Graf, D. J. Morgan, M. A. Isaacs, B. P. Reed, H. Nakajima and D. J. Payne, *Surf. Interface Anal.*, 2026, **58**, 54–65.
90 L. Li, T. Wang, B. Hu, L. I. Oldham, Q. Chen, K. Li, C. Yang, P. Alimard, Z. Meng, H. Ning, J. R. Durrant, A. Kafizas and A. A. Bakulin, *J. Am. Chem. Soc.*, 2026, **148**, 26322–26332.

